# Experimental Benchmarking of Next-Gen Indoor Positioning Technologies (Unmodulated) Visible Light Positioning and Ultra-Wideband

Sander Bastiaens, Jono Vanhie-Van Gerwen, Nicola Macoir, Kenneth Deprez, Cedric De Cock, Wout Joseph, *Senior Member, IEEE*, Eli De Poorter, and David Plets, *Member, IEEE*

***Abstract*—Within the context of the Internet of Things (IoT), many applications require high-quality positioning services. As opposed to traditional technologies, the two most recent positioning solutions: 1) ultra-wideband (UWB) and 2) (unmodulated) visible light positioning [(u)VLP] are well suited to economically supply centimeter-to-decimeter level accuracy. This manuscript benchmarks the 2-D positioning performance of an 8-anchor asymmetric double-sided two-way ranging (aSDS-TWR) UWB system and a 15-LED frequency-division multiple access (FDMA) received signal strength (RSS) (u)VLP system in terms of feasibility and accuracy. With extensive experimental data, collected at two heights in a 8 m by 6 m open zone equipped with a precise ground-truth system, it is demonstrated that both visible light positioning (VLP) and UWB already attain median and 90$^{th}$ percentile positioning errors in the order of 5 and 10 cm in line-of-sight (LOS) conditions. An approximately 20-cm median accuracy can be obtained with uVLP, whose main benefit is it being infrastructureless and thus very inexpensive. The accuracy degradation effects of non-LOS (NLOS) on UWB/(u)VLP are highlighted with four scenarios, each consisting of a different configuration of metallic closets. For the considered setup, in 2-D and with minimal tilt of the object to be tracked, VLP outscores UWB in NLOS conditions, while for LOS scenarios similar results are obtained.**

***Index Terms*—Experiments, indoor localization, indoor positioning, ultra-wideband (UWB), unmodulated visible light positioning (uVLP), visible light positioning (VLP).**

## I. Introduction

With the all-pervading Internet of Things (IoT) paradigm enabling consumer location-based services, Industry 4.0, Smart Architectures, Health 4.0, Agriculture 4.0 and Fifth-generation technology applications that all demand high-quality positioning services, indoor positioning systems (IPSs) are garnering significant interest [1]. Besides for applications, such as asset tracking, navigation, and virtual reality, accurate localization plays a vital role in IoT devices, offering preference management, privacy, security, and safety. However, with the legacy IPSs unable to ensure a sufficient quality of positioning service (QPoS), the indoor location market's vast potential remains largely untapped [2].

Particularly, the tracking of (unmanned) vehicles, such as the robots or forklifts found in industry, the hospital beds or equipment carts in healthcare, and the shopping carts in retail, is still demanding IPSs that deliver decimeter-level accurate tracking at a very low cost or couple a highly available centimeter-level navigation with a low to medium price tag. The traditional radio frequency-based IPSs do not accuracy-scale due to self-interference and/or interference with the (existing) communication infrastructure. The two most recent competitors, ultra-wideband (UWB) and visible light positioning (VLP) are better suited. The former scales comparatively well due to its interference minimization, the latter by virtue of its vast license- and congestion-exempt spectrum.

UWB minimizes interference by transmitting (sub)-nanosecond modulated pulse signals that have a low and well-regulated effective isotropic radiated power. The high temporal resolution allows to accurately measure the signal's time of flight (TOF) and to finely resolve the multipath components in the channel impulse response (CIR). The associated real-time, centimeter-order positioning renders UWB one of the most promising IPS technologies to date [3], as attested by its sprouting commercial deployments and its integration in high-end smartphones. The latter enables a swift interfacing with IoT devices. Moreover, UWB-enabled location-aware sensor networks dispose of a power-efficient, jamming and interception resilient, encrypted communication means that permits both collaborative localization and localization with respect to a quickly deployed reference infrastructure. For UWB, ToF-based asymmetric double-sided two-way ranging (aSDS-TWR) is the dominant localization principle, trading-off practicality, latency and accuracy [3]. It mitigates the degrading effect of clock drift, without requiring time synchronization and without a large message overhead.

As a smart lighting application, VLP profits from both light-emitting diodes (LEDs) becoming ubiquitous, i.e., the *solid-state lighting revolution* [4], and the advent of the Light(ing) as a Service (LaaS) business model, i.e., introducing service differentiation in a provider-maintained lighting infrastructure. VLP inexpensively infers accurate positioning by demultiplexing the unnoticeably (intensity) modulated LEDs' photocurrent contributions. Its main economic driver is based on the

Manuscript received 25 October 2021; revised 14 February 2022; accepted 17 March 2022. Date of publication 23 March 2022; date of current version 7 September 2022. *(Corresponding author: Sander Bastiaens.)*

Sander Bastiaens, Kenneth Deprez, Cedric De Cock, Wout Joseph, and David Plets are with the Research Group WAVES, Department of Information Technology (INTEC), Ghent University/imec, 9052 Gent, Belgium (e-mail: sander.bastiaens@ugent.be).

Jono Vanhie-Van Gerwen, Nicola Macoir, and Eli De Poorter are with the IDLab Research Group, INTEC, Ghent University/imec, 9052 Gent, Belgium.

Digital Object Identifier 10.1109/JIOT.2022.3161791

concurrent use of (part of) the existing illumination infrastructure. Already supporting pulse-width dimming, LEDs can easily be wielded for square-waves-based frequency-division multiplexing access (FDMA) [5]. VLP's benefits include its minimal contribution and relative immunity to electromagnetic interference, and its limited transmission range that entails safety and privacy [4]. The wide applicability, high coverage, aptitude for energy efficiency and harvesting, smartphone compatibility, and substantial receiver-side scalability are also appealing to IoT applications.

Unfortunately, the dual lighting-positioning functionality frequently necessitates infrastructure modifications, generally by means of a LED driver retrofit, and/or the addition of VLP-enabled or illumination-specific infrastructure. The idea behind unmodulated VLP (uVLP) is to work with light signals of opportunity (LSOOP) [6], i.e., with unmodified light sources, to target decimeter-level accuracy applications where the economics matter most. In fact, as LEDs are prevalent in indoor spaces [4] and used as-are, uVLP's pricing is restricted to the receiver's cost, which is in itself a bargain.

Weight, cost, and energy-constrained (u)VLP systems frequently resort to received signal strength (RSS) positioning with a single photodiode (PD), instead of camera-based angle of arrival (AOA). A PD's larger bandwidth is well suited to demodulate the LEDs' characteristic frequency (CF) in uVLP, and for applications in need of a significant location refresh rate and stroboscopic effect robustness [7]. Moreover, (u)VLP's limited receiver complexity permits its use as either a dedicated or Li-Fi-inherent location service with IoT devices. Its broadcasting nature enables the constrained IoT devices to query their location at their own incentive.

Although both UWB and (u)VLP show promise, it is arduous to diligently benchmark the two based on literature results. This is a problem well known in indoor localization [8], where the results depend on the irreproducible roll-out and where vital parameters are not necessarily disclosed. The roll-out environment, how many anchors of what type it is equipped with, which calibration is performed, the localization parameters, and even the used result metric, all affect the positioning outcome [9]. Furthermore, the localization data generally have been collected sparsely and/or in a small lab setup [10]. This is especially the case for (u)VLP. The organization of indoor positioning competitions [11] helps, but these have only recently started to incorporate UWB tracks and have yet to consider VLP.

In response, this manuscript compares the current 2-D positioning performance of aSDS-TWR UWB [12], [13] and RSS-based (u)VLP [6]. Hereto, a 11 m $\times$ 8 m open zone is equipped with 15 VLP-enabled point source-like LEDs, eight UWB anchors, and eight motion capture (MoCap) cameras that supply the highly accurate ground truth. With both the (u)VLP PD receiver and the UWB tag placed on a height-adjustable cart, stateless [i.a., multilateration] and stateful (Kalman filter) localization is performed at two heights in line-of-sight (LOS) conditions. In addition, the open zone is furnished with various configurations of metallic closets to study the performance degradation of UWB and (u)VLP in the presence of non-LOS (NLOS). The influence of anchor selection and the prior calibration effort is also studied.

Concretely, this article's contributions are summarized as follows.

1) An extensive experimental evaluation of the 2-D positioning performance of aSDS-TWR UWB and RSS-based (u)VLP with a single PD in the same LOS and NLOS conditions with respect to a highly accurate MoCap ground-truth system.
2) Both the accuracy and precision of ranging, stateless and stateful localization, are investigated.

## II. Related Work

### A. UWB Research

UWB positioning is mostly associated with time difference of arrival (TDOA) and TOF, though standalone/hybrid AOA appears [3]. Despite TOF's higher energy consumption, it is generally favored to TDOA, which has anchor synchronization via a timing cable as prerequisite. Building on advancements in transceiver design, low-level communication protocols and propagation models [14]–[16], UWB research has/is mainly focused on both autocalibration [17] and improving the ranging and localization accuracy by accounting/correcting for range bias and for NLOS contributions.

Originating from nonideal antenna radiation patterns, diverging transmitter powers, pulse shape distortion, clock drift, hardware timing inconsistencies, installation errors, ..., [18], range bias can be RSS and/or distance-dependent and is normally calibrated to great effect. The performance degradation effect of NLOS, of multipath, obstructions, and excess delay, is combated by adequate LOS path detection algorithms [19], and NLOS estimation and compensation [20], [21] by means of signal statistics [22], manual calibration [23], models of the expected ranging error [24], or machine learning [25].

Though open source UWB platforms are emerging [13], most UWB systems in the literature are of commercial nature. These (commercial) UWB solutions typically claim a sub-decimeter and a 10–30-cm positioning accuracy in indoor LOS and NLOS conditions, respectively. Scientific literature learns that in larger, NLOS-harsher environments their accuracy curtails, with the extent dependent on the type of environment and UWB solution [21], [26], [27].

### B. VLP Research

The nascence of VLP is apparent from the diversity in the positioning system principles being developed, the limited offering of commercial systems, and the lack of evaluations of large-scale deployments [28]. Positioning can be offered as part of a communication network [29] or preferably as a standalone service with a camera [30] or PD [7] receiver, and with either an RGB-composed or a phosphor-based LED, or a diffused laser diode. VLP systems are generally simplex, i.e., broadcasting signals from the LEDs to a PD receiver.

Though T(D)OA is possible for VLP, it is not prevalent due to both the limited LED bandwidth restraining the achievable timing resolution, and the required synchronization

effort associated with typically dense transmitter deployments. Helped by the absence of small-scale fading and the more spatially confined NLOS influence, RSS-based VLP is capable of centimeter-to-decimeter accuracy, only needing a single PD.

Range/location bias manifests for RSS VLP as well, in the form of nonideal (Lambertian) acceptance [7] or radiation patterns [31], of tilting and of time variations on the radiant power, whether present purposefully with dimming or not [32]. The bias factors are frequently (arbitrary) calibration fitted at once [33] or indirectly learned with machine learning models based on tedious *in-situ* measurements [34]. However, these manual measurements are superfluous when properly modeling [7]. Range/location errors are also incurred due to LOS blockage, attenuation/refraction with partially opaque objects, and reflections-induced NLOS that is moreover not easily mitigated being devoid of an accurately determined CIR.

Evaluations of VLP are principally constricted to small lab setups, with (some of the) more detailed PD-based evaluations, showing a median positioning error in either the 1.5–6 cm or the 10–34-cm range depending on how closely the setup resembles a practical environment [7], [33]–[36].

### C. uVLP Research

uVLP systems that combine DC illuminance measurements with dead reckoning provide meter-level positioning [37]. However, their feasibility hinges on the presence of an illuminance gradient. As in lighting design a uniform illuminance is strived for, it is beneficial to decompose the total illuminance into its individual LED contributions by identifying distinguishable characteristics of light sources [6], [38], certainly when external ambient (sun) light is present. In [38], it was demonstrated that the fluorescent light's inverter induces a resonance, a CF, that allows a 90$^{\text{th}}$ percentile $p_{90} = 37$ cm accurate smartphone localization. A CF also manifests for (switched-mode) constant current LED lamps [6]. Depending on the required update rate, either a decimeter median error $p_{50}$ or a $p_{50} = 5$ cm ($p_{90} = 10.6$ cm) can be obtained. The same demodulation and positioning techniques can be applied for (u)VLP, but reaching optimal performance may require tailoring, as uVLP typically deals with a lower signal-to-noise-ratio (SNR) and requires more robust localization due to the time instability of the CF.

## III. Materials and Methods

The UWB testbed under consideration is located in the industrial IoT (IIoT) lab [10] and is equipped with additional illumination LEDs, to assess and compare the positioning performance of RSS-based (u)VLP and aSDS-TWR UWB. The testbed is schematically and photographically visualized in Fig. 1. The localization benchmarking is limited to the 8 m by 6 m open-space zone of the lab as only there accurate ground truth is available [10].

### A. aSDS-TWR UWB System

The UWB tracking system under test comprises 1 tag and $N = 8$ anchors. The anchors are rectangularly distributed over

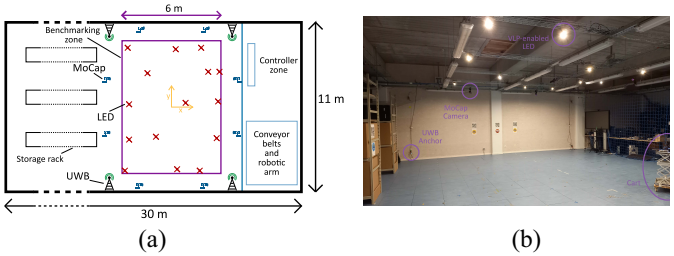


Fig. 1. (a) Schematic visualization and (b) photograph of the IIoT testbed, equipped with 15 VLP-enabled LEDs, eight UWB anchors, and a MoCap infrastructure. The evaluation zone is indicated in purple in (a).

TABLE I
Specifications of the UWB Infrastructure

| Anchor ID | 1 | 2 | 3 | 4 | 5 | 6 | 7 | 8 |
|---|---|---|---|---|---|---|---|---|
| $x_{S,i}$ $[m]$ | 3.98 | 3.98 | -4.05 | -4.05 | -3.96 | -3.96 | 3.89 | 3.89 |
| $y_{S,i}$ $[m]$ | 5.43 | 5.43 | 5.42 | 5.42 | -5.30 | -5.30 | -5.31 | -5.31 |
| $z_{S,i}$ $[m]$ | 0.20 | 2.42 | 0.40 | 2.61 | 0.44 | 2.64 | 0.44 | 2.65 |

the two sidewalls of the testbed forming approximately a rectangular cuboid (see Fig. 1). Their coordinates, with respect to the middle of the open zone, are listed in Table I. They are calibrated with the MoCap system of Section III-C.

The UWB hardware, *Wi-PoS*, is able to function interchangeably as tag and anchor by combining a Decawave DW1000[1]-based UWB transceiver [13] and a Zolertia RE-Mote[2]-based sub-GHz radio for control plane messaging [12]. The custom UWB transceiver covers channel 3 of the IEEE802.15.4a standard with an external monopole antenna, which betters Decawave's antenna's system fidelity factor and return loss [39]. The aSDS-TWR protocol runs in tandem with the energy-optimized time-division multiple access scheme detailed in [12] with no POLL/FINAL optimization. The remotely controllable UWB data rate, preamble length, pulse repetition frequency and antenna delay are set to 850 kb/s, 512 symbols, 64 MHz, and 16 476 ticks, respectively. With these messaging parameters, a range is available at an approximated 2.6 Hz rate. The antenna delay is taken as an average of a couple of devices, and no further, not DW1000-included, calibration is performed.

Upon each ranging update, the UWB location is estimated both stateless with two basic algorithms, namely, linear least-squares multilateration (MLAT) and ranging-based model-based fingerprinting (MBF) [7], and stateful with a real-time extended Kalman filter based on the discrete time white noise acceleration movement model specified in [40]. The latter is referred to with "KF." Its standard deviation on the independent in-plane acceleration and ranging measurement equals 20 cm/s$^2$ and $3 \cdot 2$ cm, respectively. The latter is based on later static measurements.

The location update rate approximately amounts to 21 Hz. The employed MBF approach entails finding the closest match between the vector holding the latest range estimation $[\widehat{d}_i]$, $i = 1..N$ per anchor and a map holding the actual ranges $d_i$ per 2.5-cm spread grid location. The closest match is found by minimizing the mean squared error cost function

[1]https://www.decawave.com/product/dw1000-radio-ic/
[2]http://zolertia.io/product/hardware/re-mote

TABLE II
SPECIFICATIONS OF THE (U)VLP INFRASTRUCTURE

| ID | $x_{S,i}[m]$ | $y_{S,i}[m]$ | $z_{S,i}[m]$ | $f_{c,i}$ [kHz] | ID | $x_{S,i}[m]$ | $y_{S,i}[m]$ | $z_{S,i}[m]$ | $f_{c,i}$ [kHz] |
|---|---|---|---|---|---|---|---|---|---|
| **1** | 1.82 | -3.58 | 2.95 | 2.0 (81.80) | **9** | -2.40 | -0.01 | 2.96 | 4.8 (78.45) |
| **2** | 0.10 | -3.45 | 2.95 | 8.0 (83.20) | **10** | 2.75 | 1.83 | 2.96 | 3.2 (79.35) |
| **3** | -2.41 | -3.64 | 2.95 | 1.6 (89.50) | **11** | 1.91 | 1.93 | 2.96 | 1.4 (85.85) |
| **4** | 2.72 | -1.86 | 2.96 | 4.0 (83.10) | **12** | -1.19 | 1.76 | 2.95 | 2.4 (85.20) |
| **5** | -1.17 | -1.78 | 2.96 | 11.2 (83.30) | **13** | 1.72 | 3.57 | 2.96 | 16.0 (92.43) |
| **6** | -2.41 | -1.80 | 2.96 | 1.0 (90.32) | **14** | 0.40 | 3.52 | 2.95 | 5.6 (85.00) |
| **7** | 2.71 | 0.07 | 2.96 | 2.8 (88.95) | **15** | -2.40 | 3.45 | 2.96 | 0.7 (79.63) |
| **8** | 0.80 | 0.05 | 2.95 | 9.6 (78.05) | | | | | |

$C(x, y) = {}^1/_K \sum_{i=1}^{K} (d_i - \widehat{d}_i)^2$. Being cumbersome, yet feasible with sparsity techniques, in terms of storage and matching latency, MBF serves at the least as a reference for nonlinear MLAT and machine learning.

Not all anchors' $\widehat{d}_i$ are required to compute a location estimate. Selecting a subset with the $K$ ($K < N$) smallest ranges might boost the accuracy. In this anchor selection, the dilution of precision was constrained to ensure that the subset always included anchors on both walls.

### B. RSS-Based VLP Roll-Out

The RSS-based VLP system under examination is a larger-scale version of the roll-out utilized in [6]. With LTM8005 Demo Boards,[3] $N = 15$ BXRE-35E2000-C-73[4] chip on board LEDs are intensity modulated to transmit square pulse trains [5]. The LEDs' planned [41] location ($x_{S,i}$, $y_{S,i}$, $z_{S,i}$), $i = 1..N$ [also shown in Fig. 1(a)] and modulation frequencies $f_{c,i}$ are displayed in Table II. To minimize inter-LED-interference, $f_{c,i}$ are assigned as to not both be odd harmonics and to preferably be an even harmonic of a ground frequency [5]. All $f_{c,i}$ exceed 700 Hz as a safeguard against flicker. 3-D printed holders ensure that the LEDs are hung level at the bottom of basket cable trays.

A single Thorlabs PDA36A2[5] PD-based receiver, in tandem with the National Instrument USB-6212 DAQ[6], localizes itself based on the per-LED demodulated photocurrent contributions $I_{PD,i}$. These $I_{PD,i}$, i.e., the RSS values, are computed via peak magnitude identification on the fast Fourier transform-based spectrum of the, with $N_S = 2560$ samples at a 256 kHz rate, discretized photocurrent signal $I_{PD}(t)$. 4 $I_{PD,i}$ samples are averaged to ensure a UWB-comparable 25 Hz update rate. The PDA36A2 is equipped with Thorlabs' FESH0750 Shortpass Filter[7] to negate the infrared contribution of the MoCap system. Its transimpedance gain is set to $1.51 \cdot 10^5$ V/A or $4.75 \cdot 10^4$ V/A depending on the vertical PD-LED distance.

For a consistent analysis, VLP also employs MLAT, MBF and KF, in combination with LED selection. The standard VLP propagation model [28] is modified to accommodate a square receiver acceptance described by $\psi_{3dB} = 0.74$ rad for the PDA36A2-FESH0750 combination, see [7] for details. In contrast to TWR UWB updating a range at a time, RSS-based VLP calculates its location estimate at once upon a $I_{PD,i}(t)$ measurement. As a consequence, the actual interpretation of the algorithms differs: 1) MBF's cost function is the Manhattan distance on $\{I_{PD,i}\}$ instead of on $\{d_i\}$; 2) the $K$ LEDs with the largest normalized $\{I_{PD,i}\}$, i.e., $\{{}^{I_{PD,i}}/_{(M \cdot P_{t,i} \cdot R_p)}\}$ [6] are selected while avoiding collinear LEDs; and 3) UWB's EKF is replaced by a fading memory linear Kalman filter with coefficient $\alpha$ [42]. It strictly acts on an MBF/MLAT positioning estimate. $\alpha$ satisfies 1.01. The Kalman filter's process and measurement noise standard deviation are equal to 20 cm and what is measured in Section IV-A4, respectively. Both the time step and process standard deviation scale with the number of averaged $I_{PD,i}$.

[3]https://www.analog.com/en/products/ltm8005.html#product-overview
[4]https://www.bridgelux.com/products/v-series
[5]https://www.thorlabs.com/thorproduct.cfm?partnumber=PDA36A2
[6]https://www.ni.com/pdf/manuals/375196d.pdf
[7]https://www.thorlabs.com/thorproduct.cfm?partnumber=FESH0750

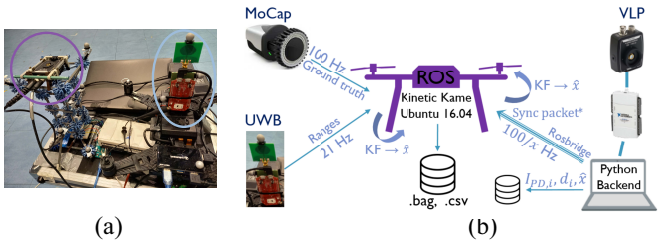


Fig. 2. Photograph and schematic representation of the integrated drone platform, placed on top of a height-adjustable cart. In (a), PD receiver and UWB tag are indicated with purple and light blue, respectively. In (b), $I_{PD,i}$ and $d_i$ refer to the RSS value and range estimate from/to anchor $i$. $\hat{x}$ and 'KF' denote the location estimate and the Kalman filter positioning approach, respectively (III).

VLP requires the calibration of: 1) the LED locations by the MoCap system (Section III-C) tracking a marker on a cord suspended from the LED and 2) the LEDs' weighted radiant power $M \cdot P_{t,i} \cdot R_p$ with $\{I_{PD,i}\}$ measurements performed directly under each LED for a 0.5 m receiver height.

During uVLP, the LTM8005 Demo Board is bypassed and no explicit modulation is performed. In uVLP, the calibration therefore also serves to chart the $f_{c,i}$ used for demodulation, which are listed between brackets in Table II. As $N_S$ is doubled to better separate the $f_{c,i}$, only 2 $\{I_{PD,i}\}$ measurements are averaged to maintain the 25-Hz update rate. Our previous analysis [6] already showed that this update rate in conjunction with the time-varying nature of uVLP does not allow a subdecimeter accuracy.

### C. Ground Truth via Motion Capture

Eight *Qualisys Miqus M3* infrared MoCap cameras[8] provide the millimeter-level accurate ground truth for the (u)VLP-UWB localization experiments [10]. Their approximated locations are shown in Fig. 1(a). The to be tracked objects, namely, the PDA and the UWB tag, are fitted with Qualisys' white markers, as can be seen in Fig. 2(a). Both the VLP and the UWB receiver are simultaneously and accurately tracked across a zone exceeding 8 m by 6 m with an update rate of 100 Hz and a typical precision of about 60 μm.

### D. System Integration on Drone

The MoCap ground-truth system, in the form of the Qualisys Track Manager[9], the UWB tag and the (u)VLP receiver all interface with the Intel Aero Compute Board of an Intel Aero Ready to Fly Drone[10], running the *Kinetic*

[8]https://www.qualisys.com/cameras/miqus/
[9]https://www.qualisys.com/software/qualisys-track-manager
[10]https://www.dji.com/be/matrice100

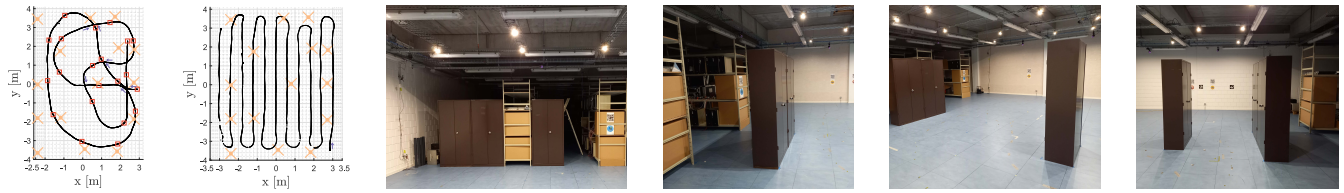


Fig. 3. Visualization of the considered (a) route and (b) zigzag (LOS) evaluation trajectory, and of (c)–(f) four NLOS scenarios with metallic closets. In the former two, the purple arrows indicate the walking direction. The boxes in (a) represent the static measurements' locations.

*Kame* distribution of the *Robot Operating System* (ROS) on top of Ubuntu Xenial Xerus (16.04). Fig. 2 visualizes this interfacing and the associated data streams, both schematically and via a photograph. The UWB tag is mounted directly on the drone. Only supported from Ubuntu Bionic Beaver (18.04) on, rather than upgrading operating system, at this time, the DAQ for VLP was addressed with a laptop and connected to ROS via Rosbridge. To limit Wi-Fi traffic, for (u)VLP, instead of the raw $I_{PD,i}(t)$ or $I_{PD,i}$, a synchronization (sync) packet is published to the ROS master on the drone with i.a., the measurement epoch and an identifier. Python 2.7-based publish/subscribe scripts gather/generate the UWB ranges, the VLP sync packet, and the location data. All this measurement data are then collected and stored in a Rosbag.

The reason behind the on-drone integration is threefold: 1) all data are timestamped by the same system; 2) ROS allows easy migration to other robotic platforms; and 3) it provides a wireless and extendible flight platform (see Section V).

### E. Evaluation Method

The drone, with the UWB tag and the VLP receiver chain, is placed on top [see Fig. 2(a)] of the height-adjustable cart, visible at the right-hand side of Fig. 1(b). Furthermore, as seen in Fig. 2(a), to counter a significant height difference between both receivers, the PD is placed on a K'nex tower.

The UWB and VLP estimates are collected during repeated slow-paced strolling with the cart along both the winding route (R) and the zigzag (Z) trajectory visualized in Fig. 3(a)/(b). These trajectories are designated with a tape on the floor for reproducibility. Attaching a string with about a 1.5 m length to the cart allows minimizing the influence of the human body when maneuvering. The positioning accuracy is evaluated at approximately 0.5 and 1.15-m receiver height, i.e., 0.52/1.17 m for VLP and 0.55/1.17 m for UWB, both in LOS-dominated conditions and in environments where NLOS is purposely introduced through the addition of metallic closets. To study the impact of reflections and obstructions, the four configurations of Fig. 3 are considered. They are as follows.

1) Three closets in series outside of the positioning zone and close to two anchors.
2) Two linked closets at the side of the zone.
3) An extension of 2) with a third closet to form a wide corridor.
4) A closer hallway with the third closet moved closer to the 2 linked closets.

Adhering to good practices [9], the employed accuracy metrics are the $50^{\text{th}}/75^{\text{th}}/90^{\text{th}}/95^{\text{th}}$ percentile $p_{50}/p_{75}/p_{90}/p_{95}$ of the 2-D Euclidean distance between the estimated and the closest-in-time ground-truth locations. As there is no exact synchronization, per location estimate, the two closest-in-time ground-truth locations are interpolated based on the timestamps involved. In characterizing the NLOS influence, spatially confined versions of the positioning metrics will be reported that only account for the one meter neighborhood of the obstacles. To evaluate the similarity between the actual and estimated trajectory, the Euclidean distance on the dynamic time-warped trajectories (denoted by DTW) and the related discrete Fréchet distance (FD) are utilized. In addition, with 21 static measurements taken along the route trajectory at the locations indicated in Fig. 3(a), the proportion of the positioning error that can be attributed to noise, i.e., the precision, rather than to bias errors, i.e., the accuracy, is studied as well. In line with [8], it is specified that in the testbed (Fig. 1), a Wi-Fi network is active, that no ambient light is present, and that the left and right wall are made up from brick and wood, respectively.

## IV. Experimental Results

### A. UWB and (u)VLP in LOS-Dominated Conditions

Fig. 4 visualizes the dynamically measured spatial distribution of the UWB [in Fig. 4(a)/(b)] and VLP [in Fig. 4(c)/(d)] MLAT/MBF and KF LOS positioning estimates for the route (R) trajectory with the receivers being located approximately (a)/(c) 0.5 m and (b)/(d) 1.15 m above the ground. The MoCap-based ground-truth trajectories are colored in black. Table III lists all the LOS experiments' associated $p_{50}$, $p_{75}$, $p_{90}$ and $p_{95}$ when UWB's $K$ is fixed to 8 and VLP's $K$ amounts to 3 and 4 for MLAT and MBF/KF, respectively.

Both UWB and VLP show a good correspondence with the ground truth. However, comparing their respective figures, a different error profile can be remarked. While UWB's error profile is largely irrespective of the location, the VLP trajectories exhibit a select few small areas where the position estimates consistently diverge from the ground truth. An example of the latter is located near the bottom of Fig. 4 (c)/(d), i.e., near LED 2 (Table II). These location-dependent bias errors mainly result from the actual propagation differing from the modeled, e.g., due to tilt of the LEDs, inter-LED-interference, etc.

*1) One-Shot Localization:* Table III allows comparing one-shot UWB and VLP, i.e., without tracking the receiver state.

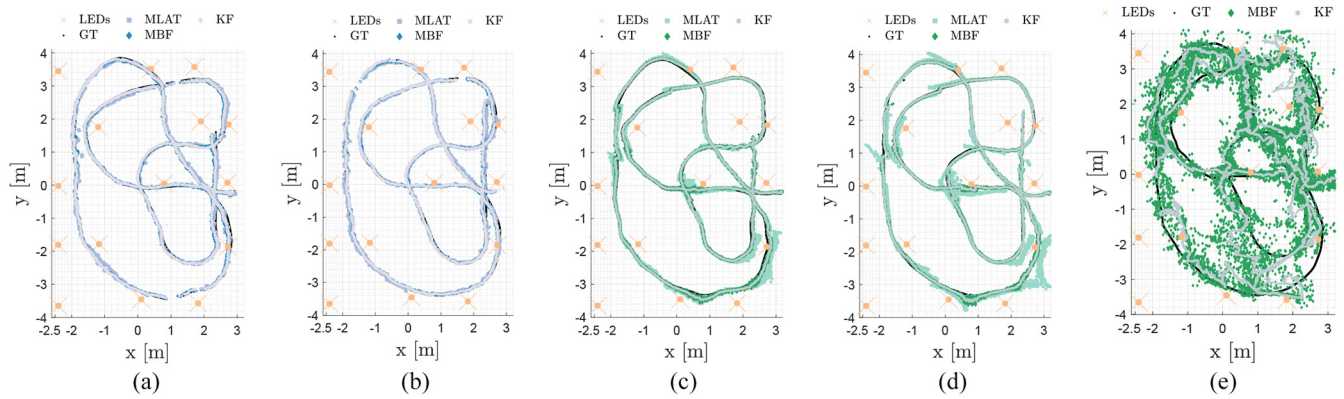


Fig. 4. Spatial distribution of the UWB (in the blue shades) and VLP (green shades) MLAT/MBF and KF positioning estimates for the winding route trajectory at approximately (a)/(c) 0.5 m and (b)/(d) 1.15 m receiver height. (e) uVLP's trajectory at the 0.5 m height. In each subfigure, the ground truth is represented in black, while the LEDs are indicated with orange.

TABLE III
UWB AND (U)VLP LOS ACCURACY FOR THE ROUTE/ZIGZAG TRAJECTORY ("MLAT" = MULTILATERATION, "MBF" = MODEL-BASED FINGERPRINTING, AND "KF" = KALMAN FILTERING)

| | | **UWB** [cm] | | **VLP** [cm] | | **uVLP** [cm] |
|---|---|---|---|---|---|---|
| | | Height 1 | Height 2 | Height 1 | Height 2 | Height 1 |
| **MLAT** | • $p_{50}$ | 4.8 / 5.3 | 4.5 / 6.0 | 5.2 / 5.5 | 6.2 / 7.1 | 33.8 / 33.4 |
| | • $p_{75}$ | 6.9 / 7.7 | 6.7 / 8.8 | 8.7 / 9.8 | 13.3 / 15.1 | 111.2 / 80.9 |
| | • $p_{90}$ | 9.4 / 10.9 | 8.9 / 12.9 | 14.7 / 24.1 | 27.1 / 121.4 | 226.9 / 212.7 |
| **MBF** | • $p_{50}$ | 5.5 / 5.0 | 5.1 / 5.3 | 3.9 / 3.1 | 3.1 / 4.0 | 24.3 / 24.3 |
| | • $p_{75}$ | 8.0 / 7.2 | 7.2 / 7.5 | 5.5 / 4.6 | 4.8 / 6.2 | 35.7 / 36.1 |
| | • $p_{90}$ | 10.6 / 9.7 | 9.4 / 9.9 | 7.7 / 6.3 | 7.4 / 9.3 | 65.1 / 79.2 |
| | • $p_{95}$ | 12.4 / 11.9 | 10.8 / 11.3 | 9.1 / 7.5 | 9.6 / 11.0 | 103.5 / 115.8 |
| **KF** | • $p_{50}$ | 4.7 / 4.7 | 4.1 / 4.7 | 3.7 / 2.9 | 2.9 / 4.0 | 21.3 / 22.1 |
| | • $p_{75}$ | 6.9 / 7.0 | 6.2 / 7.1 | 4.9 / 4.1 | 4.3 / 6.1 | 31.2 / 34.1 |
| | • $p_{90}$ | 9.3 / 9.6 | 8.6 / 9.5 | 7.1 / 5.5 | 6.5 / 8.7 | 60.1 / 68.6 |
| | • $p_{95}$ | 11.1 / 11.5 | 10.2 / 10.8 | 8.7 / 6.4 | 8.9 / 10.8 | 83.0 / 103.5 |

UWB scores around 5 and 10 cm in terms of the $p_{50}$ and $p_{90}$, respectively. There is no clear receiver height-dependence. For a fixed $K$, MLAT improves/worsens upon MBF's accuracy for the route/zigzag trajectory. Based on these measurements, overall, MBF seems slightly more robust. Another advantage is that its cost function can be (dynamically) tuned per application. However, both do not outweigh the additional complexity requirement.

Within VLP, MBF vastly outscores MLAT (Table III), in terms of accuracy and robustness. This gain is a consequence of MBF pairing a noninvertible propagation model, which i.a., incorporates a well-modeled receiver acceptance [6] to more closely fit with the actual propagation, with an RSS-based, instead of a range-based, cost function. MBF-based VLP is able to supply a $p_{50}$ and $p_{90}$ accuracy significantly better than 5 and 10 cm, respectively. On average, the $p_{50}$ and $p_{90}$ amount to 3.5 and 7.7 cm. In contrast, MLAT with the ideal Lambertian propagation model proves to be inapt for navigation. Positioning outliers manifest as "jumps" due to handover (associated with $K = 3$). Its $p_{75}$ already nears or exceeds 10 cm.

MBF does not clearly manifest a height-dependence despite that theoretically, within bounds, the higher SNR and the lower impact of limited tilts should enable more accurate estimation when the receiver is closer to the lamp. This suggests that the performance is dictated by both the receiver tilt variation between tests and the inter-LED-interference present. For MLAT, the significant disparity between the modeled and actual propagation being more pronounced at larger incidence angles effectuates a larger positioning error at height 2 [6].

Three additional remarks about VLP have to be made.

1) The presence of MLAT (handover) outliers can be reduced by utilizing a larger $K$. However, the mentioned divergences of the propagation model then cause an overall accuracy degradation.
2) The latency and complexity of MBF may prohibit its use for high-update applications. Instead, MLAT based on a fitted power law version of the propagation model, comes at an acceptable $p_{50}/p_{75}/p_{90}$ cost of 0.6 cm/0.9 cm/1.7 cm with respect to MBF, for the winding route trajectory and the 0.5 m height.
3) In this analysis, the PD's minimal tilt, invariably present by its installation, was not compensated. When the propagation model accounts for a 1 ° rightwards tilt, perpendicular on the movement direction, MBF's $p_{50}/p_{75}$ improves to 2.5/5.0 cm for the route trajectory and height 0.5 m. The associated $p_{90}/p_{95}$ equals 5.6/7.9 cm. The MBF estimates now visibly better match the ground truth (not shown), certainly in the neighborhood of LED 2.

*2) Stateful Localization:* Fig. 4 and Table III show the accuracy-boosting effect of the (extended) Kalman filtering on the $p_{50}$ and $p_{75}$. Averaged over both heights and both trajectories, for UWB, KF effectuates a substantial $p_{50}/p_{75}$ reduction of approximately 11%/9% over MLAT. At larger moving velocities and with tailored filters, this reduction will be even more pronounced. Filtering the VLP MBF's estimates also unambiguously brings $p_{50}/p_{75}$ and $p_{90}$ benefits of 5%/8% and 10%. Kalman filtering also generally enlarges the similarity between the estimated and the ground-truth trajectories. For VLP, at heights 1 and 2, respectively, KF reduces MBF's cumulative DTW error by 9% and 18%, while the associated FD drops by 23% (to 19.9 cm) and 36% (to 20.1 cm). In

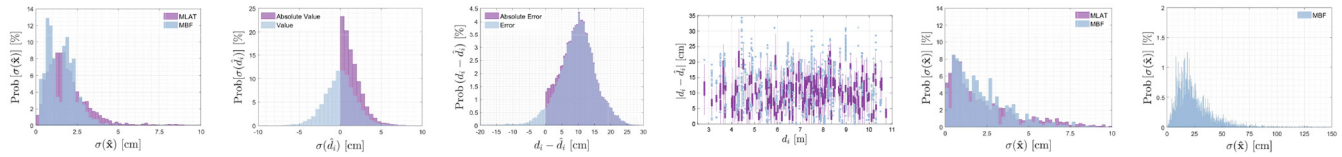


Fig. 5. Histogram representation of the stationary measurements' UWB (a) location precision, (b) ranging precision and (c) ranging error, and (e) VLP and (f) uVLP location precision. (d) All UWB anchors' joint ranging errors over the ground-truth tag-anchor distance with bar plots.

regions with several consecutive outliers, the KF may locally accentuate the following nonbias errors in the immediate vicinity. It should be remarked that the swapping of the filter approaches of UWB and VLP does not offer benefits. Hence, nor using a batch version of the EKF with the VLP ranges, instead of the VLP locations-based linear KF, nor the linear KF ($\alpha = 1.01$) with the UWB location estimates, instead of the UWB ranges-based EKF, improves the positioning.

In 2-D and without receiver tilt, both VLP and UWB thus definitely attain the prototypical 5-cm median and 10-cm $p_{90}$ accuracy bounds in LOS conditions, frequently demanded by the envisioned applications. Though, in a practical deployment, a $p_{50}/p_{90}$ penalty will likely be incurred due to the inaccurate charting of the anchor coordinates [41]. This partially explains why this manuscript's LOS errors are lower than, or comparably to, those reported in calibrated small-scale lab setups [3], [6], [10], [28]. Whereas at this point, VLP (marginally) outscores UWB, a detailed UWB/VLP aptitude assessment still necessitates a quantification of both the accuracy in harsher environments and the other QPoS [2] indicators.

Nor current UWB nor contemporary VLP roll-outs are suited for the very cost-constrained applications. That is where uVLP will come into play.

*3) Unmodulated VLP:* Previously investigated for a controlled 4 LED roll-out [6], Table II and Fig. 4(e) attest that the uVLP principle extends to a larger scale. With the exception of LEDs 2 and 4, the LEDs' $f_{c,i}$ are adequately spread in frequency to support update rates exceeding 100 Hz. On account of employing LSOOP, i.e., time-varying spurious signals with a low SNR, uVLP is distinctively more inaccurate and imprecise than VLP/UWB, as is shown in Table III. Nevertheless, analogous to [6] and at height 1, MBF-based uVLP's $p_{50}$, $p_{75}$, and $p_{90}$ still equal 24.3, 35.7, and 65.1 cm, respectively. The zigzag trajectory sees similar results, e.g., a $p_{50} = 24.3$ cm. Stateful localization even ameliorates the $p_{50}$, $p_{75}$ and $p_{90}$ by 12% (to 21.3 cm), 13% (to 31.2 cm), and 8% (to 60.1 cm). Importantly, uVLP then enables a $p_{75}$ around 30 cm, a typical target for tracking applications.

These experimental accuracies are hindered by the presence of a spatial region with substantial positioning outliers, not coincidentally located around LEDs 2 and 4. Both are indicated in red in Fig. 4(e). There, the accuracy degradation is caused by $I_{PD,i}$ leakage between both LEDs as a consequence of the $N_S$ required for a 25-Hz update rate not being sufficient in the presence of the time-varying nature of both $f_{c,i}$ and the $I_{PD,i}$ magnitude at $f_{c,i}$. It should be noted though, as is outlined in [6], that both lowering the update rate and tailoring the demodulation, i.e., the measurement interval $N_S$ and the number of $I_{PD,i}$ to average, have a significant accuracy boosting benefit (to a 5-cm $p_{50}$ [6]). Even with a $p_{75} \sim 30$ cm, uVLP's differentiation in cost represents its application potential, especially for low-cost tracking.

*4) Localization Precision via Static Measurements:* By means of the static measurements at both heights, Fig. 5 provides insight regarding the location $\sigma(\hat{\mathbf{x}})$ and ranging $\sigma(\hat{d}_i)$ precision of UWB/(u)VLP. Hereto, at the 21 measurement locations, a $\sigma(\hat{\mathbf{x}})/\sigma(\hat{d}_i)$ value is computed for each of the 100 data points, which are collected every 1 s. Fig. 5(a) shows that UWB's $\sigma(\hat{\mathbf{x}})$ distribution is slightly algorithm-dependent, but Rayleigh-like. The mean of $\sigma(\hat{\mathbf{x}})$ amounts to 1.5 and 1.9 cm for MBF and MLAT, respectively. As can be viewed from the light blue curve (purple) in Fig. 5(b), the UWB ranging $\sigma(\hat{d}_i)$ ($\sigma(|\hat{d}_i|)$) exhibits a (folded) Gaussian-like distribution with an approximately zero, i.e., $-5.7 \cdot 10^{-15}$ cm (1.5 cm) mean and a 2 cm (1.3 cm) standard deviation. It is hence well suited for Kalman filtering (Section IV-A2). The skewed distribution of UWB's corresponding (absolute) 3-D ranging error is depicted in Fig. 5(c). With a 9.7 cm (10.1 cm) mean and a 5.9 cm (5.1 cm) standard deviation, $\hat{d}_i$ are typically underestimates, as opposed to the overestimates reported at longer $d_i$ due to NLOS [21]. Furthermore, Fig. 5(d) conveys that the distance-dependent ranging error bias across all anchors is limited for the $d_i$ common to this roll-out.

VLP's mean $\sigma(\hat{\mathbf{x}})$ [Fig. 5(e)] equals 2.4 cm at height 1 and 2.0 cm at height 2, respectively. It thereby exceeds UWB's values. Important to note herewith is that VLP's $\sigma(\hat{\mathbf{x}})$ manifests a substantial spatial dependence, which is not restricted to the receiver's height. A significant variance across the 2 times 21 static measurements is observable. Comparing Fig. 5(e)/(a) allows concluding that VLP's $\sigma(\hat{\mathbf{x}})$ distribution has a more pronounced tail, further diverging from a Gaussian error profile. As a side note, the positioning error data of the static measurements is in agreement with those of Section IV-A1, with VLP's still (slightly) better than UWB's. The relatively large positioning deviation of VLP can (partly) be attributed to the imperfect clock, and thus waveform, of the transmitter. Ensuring a modulator with less clock jitter, or employing a similar oscillator in the transceiver hardware, should ameliorate VLP's precision.

Finally, Fig. 5 (f) demonstrates that noise, in the form of a lower SNR and a time-varying $I_{PD,i}$, can be identified as the main responsible for uVLP's accuracy degradation compared to VLP. Its mean $\sigma(\hat{\mathbf{x}})$ at height 1 totals 26.7 cm with the standard deviation on $\sigma(\hat{\mathbf{x}})$ being of comparable magnitude.

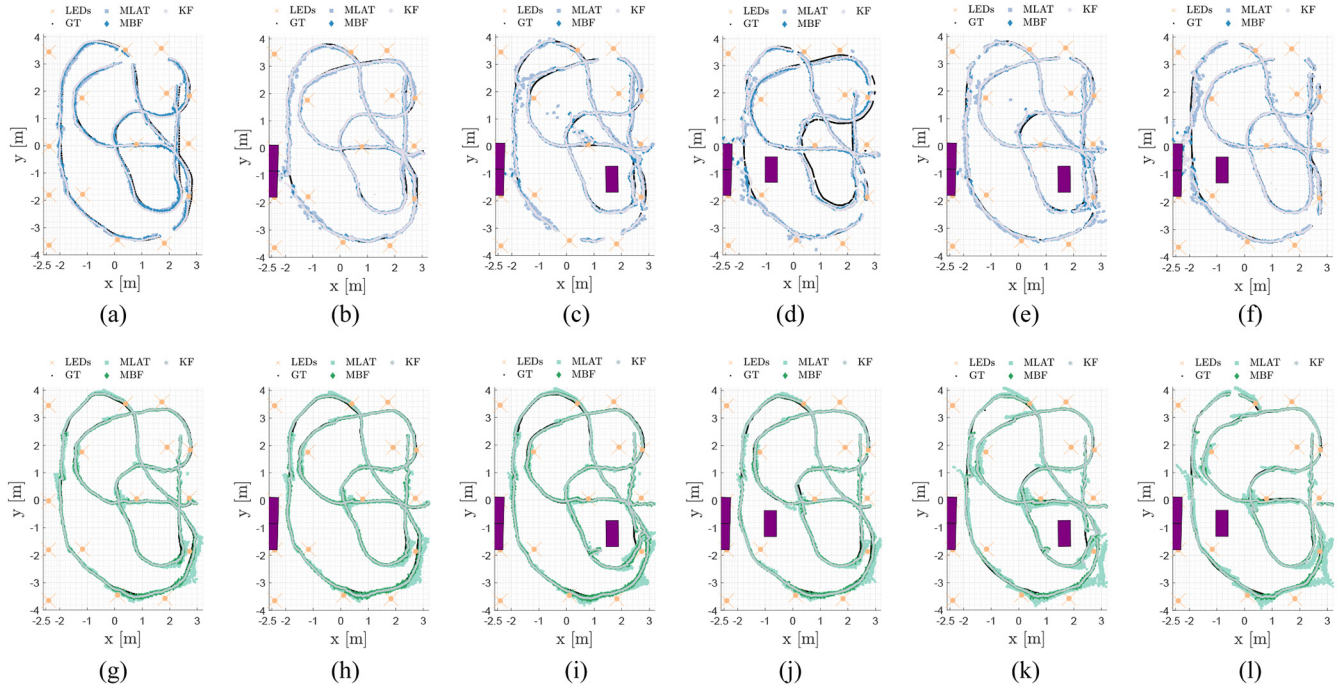


Fig. 6. Spatial distribution of the UWB (in blue) and VLP (in green) MLAT/MBF and KF position estimates in the presence of (a)–(d)/(g)–(j) the four NLOS configurations at height 1 and (e) and (f)/(k) and (l) of NLOS configurations 3) and 4) at height 2. NLOS configuration 1)'s three closets form a line segment, which falls outside the view of (a)/(g), with their fronts and the present storage rack. Its start and end point are $(-3.86\text{ m}, -4.48\text{ m})$ and $(-3.86\text{ m}, -0.81\text{ m})$.

TABLE IV
NLOS ACCURACIES OF UWB AND VLP WITH KF [IN (CM)] FOR THE MEASUREMENT SCENARIOS DEFINED IN SECTION III-E

| **Scenario** | Tech. | $p_{50}$ $(p_{50,N})$ | $p_{90}$ $(p_{90,N})$ | $p_{95}$ $(p_{95,N})$ | FD $(\text{FD}_N)$ |
|---|---|---|---|---|---|
| (i), h1 | UWB | 9.3 (-) | 13.8 (-) | 15.3 (-) | 174.7 (-) |
| | VLP | 3.0 (-) | 6.6 (-) | 7.6 (-) | 12.4 (-) |
| (ii), h1 | UWB | 5.3 (4.1) | 9.8 (13.3) | 11.4 (42.7) | 236.9 (58.3) |
| | VLP | 3.1 (2.5) | 6.8 (4.5) | 8.3 (9.2) | 14.0 (9.5) |
| (iii), h1 | UWB | 5.6 (5.2) | 11.3 (11.9) | 14.1 (19.7) | 223.9 (223.9) |
| | VLP | 4.0 (4.1) | 7.7 (8.2) | 9.6 (11.5) | 46.1 (46.1) |
| (iv), h1 | UWB | 7.4 (8.7) | 19.3 (44.7) | 25.9 (81.7) | 123.6 (123.6) |
| | VLP | 3.7 (3.7) | 7.0 (8.0) | 8.0 (9.3) | 15.0 (12.4) |
| (ii), h2 | UWB | 4.2 (3.5) | 9.4 (6.8) | 11.6 (10.0) | 239.9 (26.5) |
| | VLP | 3.0 (2.7) | 6.6 (6.8) | 8.3 (15.4) | 19.6 (21.8) |
| (iii), h2 | UWB | 5.2 (6.6) | 11.1 (13.3) | 14.5 (15.5) | 256.1 (29.2) |
| | VLP | 3.0 (3.2) | 7.6 (8.4) | 9.2 (10.7) | 51.3 (51.3) |
| (iv), h2 | UWB | 5.3 (5.2) | 11.7 (29.0) | 17.6 (40.0) | 234.7 (62.9) |
| | VLP | 3.3 (4.3) | 7.6 (10.8) | 10.4 (17.2) | 24.8 (26.6) |

### *B. Tracking in the Presence of NLOS*

The introduction of different constellations of matte metallic closets allows studying the accuracy degradation caused by obstructing, refracting, and/or reflecting obstacles. Fig. 6 depicts the UWB/VLP reconstructed trajectories when MLAT/MBF and KF positioning, in the presence of the 4 NLOS configurations of Section III-E with the receiver being located at height 1 (approx. 0.5 m). To additionally highlight the interplay with the receiver height, two of those 4 NLOS configurations are visualized for height 2 (approx. 1.15 m) in Fig. 6 as well. Table IV lists the scenario's KF-based performance metrics: the $p_{50}$, $p_{90}$, $p_{95}$, and FD with their associated $p_{50,N}$, $p_{90,N}$, $p_{95,N}$, and $\text{FD}_N$ variants that are similarly computed but only consider the data within a 1-m bounding box around the obstacles.

*1) UWB:* The extent of the NLOS accuracy degradation, to which both (u)VLP/UWB are subject to, highly depends on the distribution of NLOS-inducing objects and on the localization systems' roll-out. The top row of Fig. 6 avouches this for UWB. In Fig. 6(a), NLOS configuration 1), with the three closets close to anchors 5 and 6 (Table I), represents a well-known arduous case of obstacle placement for UWB. The limited path length, path loss and hence timing difference impedes accurately resolving the LOS from the multipath components in the anchors' CIR. As a result, the positioning significantly worsens. Though, (dynamic) anchor selection may provide an error reducing effect. (Re)moving those closets further [Fig. 6(b)] leads to a very dissimilar error profile. There, the errors are more confined to the region around the closets, with local $p_{95,N}$ errors as large as 42.7 cm. The overall $p_{50}$ still rises by 13% over the LOS case.

The addition of a third closet [Fig. 6(c)] only exacerbates the NLOS-induced error (see Table IV). Moving that closet closer to the other two, i.e., forming the corridor configuration 4) [Fig. 6(d)], not only instigates the largest $p_{90}/p_{95}$ (and $p_{90,N}/p_{95,N}$) errors found in between the closets (with $p_{90}/p_{90,N}$ up to 19.3/44.7 cm), but also causes degradation further from the obstacles due to shadowing. Configuration 4) is associated with a $p_{50}/p_{90}/p_{95}$ increase by 55/108/134%. The same NLOS phenomena occur at the second receiver height [see Fig. 6(e)/(f)], but typically with a more limited

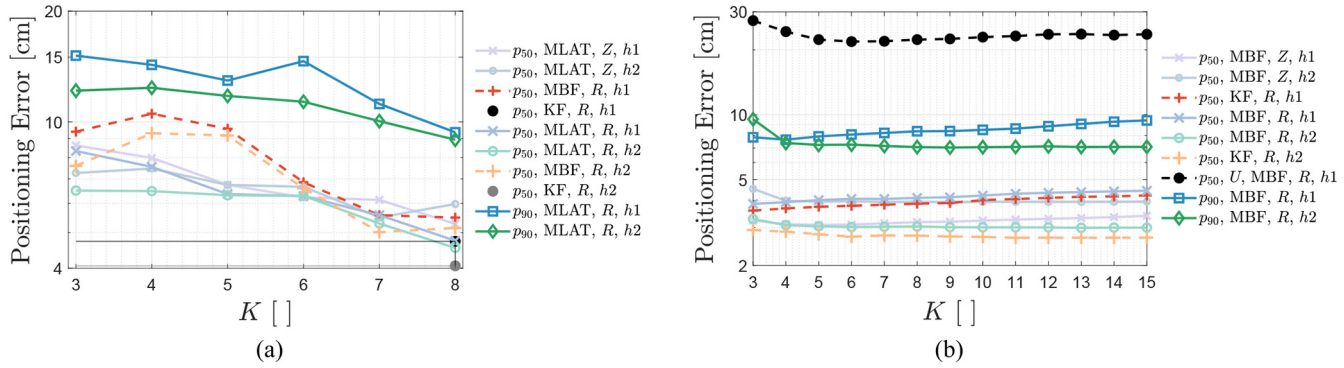


Fig. 7. Influence of the anchor selection parameter $K$ on (a) UWB and (b) (u)VLP positioning accuracy in LOS dominated environments. "R" and "Z" denote the route (Fig. 3(a)) and zigzag (Fig. 3(b)) trajectory, respectively. "U" refers to uVLP.

magnitude. The propagation paths change beneficially and the obstacle-impacted area is more confined to the closets that no longer tower above the receiver. Interestingly and counter-intuitively, the introduction of NLOS can locally ameliorate the UWB positioning by compensating the underestimation of the ranges.

*2) VLP:* The influence of NLOS on the VLP accuracy is more spatially confined to the immediate vicinity of the obstacles. Fig. 6(g) is a prime example, the closets at the side do not affect the VLP estimates in the open zone. The two conjunct closets at the side [configuration 2)] also do not induce large errors. By comparing Fig. 6(h)/(i) and (j), it can be concluded that the effect of NLOS on the positioning is vastly dependent on the (local) deployment of the LED transmitters (and thus the location of the obstacles) through the propagation angles. Particularly, the impact of the reflections at the hand of the solitary closet [Fig. 6(i) and (j)] varies, resulting for configurations 3) and 4) in a $p_{95,N} = 11.5$ and 9.3 cm, respectively. The experiments with the PD nearer to the LED [Fig. 6(k) and (l)] show the limited height-dependence of NLOS influence, when comparing to Fig. 6(i) and (j). In Table IV, some of the NLOS configurations (Table IV) evincing improved metrics over the LOS positioning (Table III) can be explained by less receiver tilt being present, while a $p_{50,N}/p_{90,N}/p_{95,N}$ reduction (compared to $p_{50}/p_{90}/p_{95}$) can be attributed to the bounding box coincidentally being a local area of good positioning.

Importantly, in the considered closet configurations, VLP still manages to attain a $p_{90} \approx 10$ cm or better. Its corresponding trajectories are also much more similar to the ground truths' than UWB's, as evidenced by considerably lower FD [and $\text{FD}_N$] values. In RSS-based VLP, significant obstacle-induced accuracy degradation typically only occurs in the immediate (1 m) vicinity of said obstacle, with the exception being LEDs that are near the obstacle. There: 1) the path difference of a selected LEDs' LOS and (mostly specular) NLOS components is limited and 2) obstruction of the LOS link is more likely to take place. These effects result in a larger or smaller $I_{PD,i}$ than expected, which generally cause the MBF position estimates to be pulled toward and pushed away from the object, respectively. As VLP is normally associated with dense LED deployments (to provide its primary illuminance function), often at least three relatively unaffected LOS links are available, i.e., except in the immediate vicinity of obstacles, such that accurate localization is ensured. Obviously, this analysis of VLP also applies to uVLP, with the difference being that uVLP is noise dominated (Section IV-A4).

*3) Conclusion:* In conclusion, both UWB and (u)VLP rollouts need to be planned weary of NLOS obstacles. For the considered setups, VLP copes well with the objects, certainly in comparison to UWB. Its $p_{95}$ remains bounded by 15.4 cm. As long as at least three unobstructed LOS links are available, light-based accuracy degradation is found near the obstacles. Mostly featuring in less dense deployments, UWB systems tend to suffer more from the multipath and obstruction brought by the obstacles. Here, a $p_{95} > 25$ cm can be induced.

It should be noted that both technologies' obstacle-added error can be alleviated with NLOS identification and mitigation techniques (Section II-A) or by fusing them with inertial measurements. The former for instance involves: 1) exploiting the temporal variance on $d_i/I_{PD,i}$ or the location variance obtained via positioning with different $d_i/I_{PD,i}$ subsets [20], [43], [44]; 2) checking whether the $d_i/I_{PD,i}$ subset coincides with a positioning cell; and 3) or network planning to avoid significant NLOS. The benefit of the UWB system is that waveform signal statistics or CIR-based LOS path detection, NLOS identification and discarding [20], [45], [46], NLOS classification and mitigation [47]–[49] algorithms dispose of additional multipath components' information [20], [50]. Fusion with inertial navigation should work especially well in areas with local and abrupt positioning outliers that will smooth out. In this chapter, additionally to what is DW1000-inherent, neither technique is applied to quantify the "raw" impact of NLOS.

Overall, whereas VLP arises more favorably accuracy-wise from these experiments, it must be stated that this conclusion will not transfer to larger velocity 3-D drone localization with receiver tilt in industrial-like environments with high ceilings. In fact, when considering the nonaccuracy QPoS pillars [2] as well, i.a., the cost/calibration (edge UWB), scalability (edge VLP) and the availability/robustness (edge UWB), the current UWB systems can be designated as better suited (and more ready) for tracking/navigating (unmanned) vehicles.

### C. Influence Positioning (Calibration) Parameters

This last result section analyses the influence of both the anchor selection parameter $K$ and the calibration level. Hereto, the trajectory data are used.

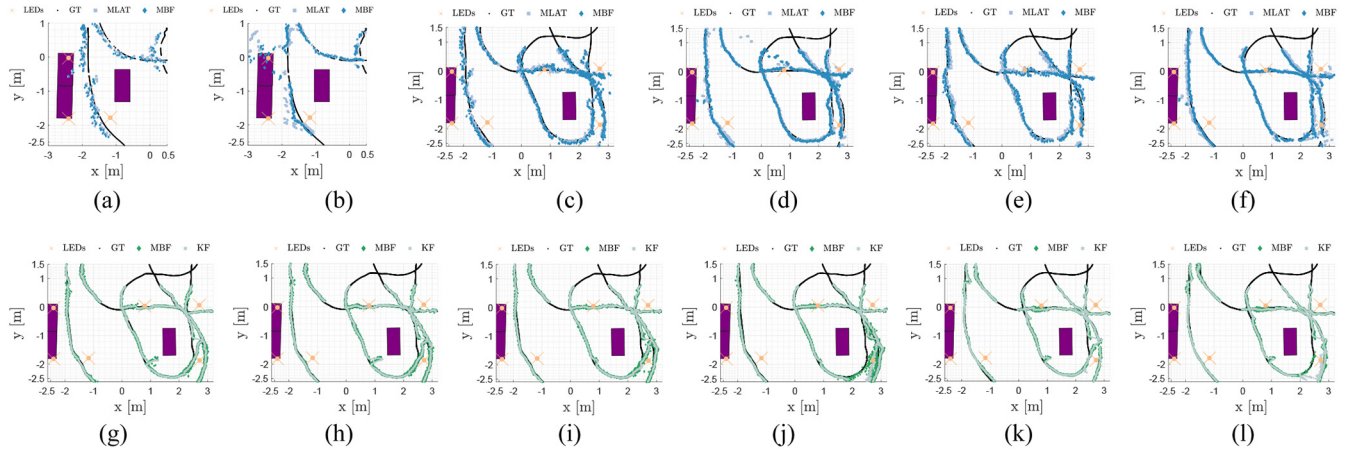


Fig. 8. UWB (top row) and VLP (bottom row) positioning in the 1 m [(a) and (b)] or 1.5 m bounding box vicinity of obstacles. For UWB, respectively $K = 3$ and $K = 8$ are wielded in the case of NLOS configuration 4 (a)/(b) with receiver height 1, and for configuration 3 in conjunction with (c)/(d) height 1 and (e)/(f) height 2. For VLP and NLOS configuration 3, PD height 1 is coupled with a $K$ equaling (g) 3, (h) 4, (i) 6, (j) 15, and height 2 with (k) 4 and (l) 15, respectively.

*1) Influence of Anchor Selection Number K:* Fig. 7(a) and (b) depicts the UWB and (u)VLP $p_{50}/p_{90}$ in LOS conditions as a function of $K$. Particularly, the UWB algorithms' appertaining $p_{50}/p_{90}$ is contingent on $K$. Typically, employing all anchors ($K = 8$) is favored. For MLAT-based (u)VLP, $K = 3$ is typically best [41], while the optimal $K$ for MBF depends on the roll-out, the receiver height, the inter-LED-interference and even the positioning metric. For these dense LED deployments, for $K > 3$, the impact of a nonideal $K$ selection is rather minor. In uVLP ["U" suffix in Fig. 7(b)], LED selection is more important, there $5 \leq K \leq 8$ is best. $5 \leq K \leq 8$ is a result of the tradeoff between averaging the $I_{PD,i}$ magnitude variation of the nearby LEDs and avoiding the $I_{PD,i}$ of more distant LEDs that have a too small SNR.

Fig. 8 emphasizes that near obstacles an adequate anchor selection is vital as well. For UWB, an elevated $K$ ($K = 8$ in Fig. 8) causes more outspoken positioning outliers, while a lower $K$ value ($K = 3$ in Fig. 8) reduces this "peaking" behavior at the cost of more spread on the positioning estimates. $K = 3$ tends to significantly improve the $p_{95,N}$ (and $p_{90,N}$), but effectuates a substantial incrementing $p_{50,N}$ as well. The optimal $K$ hence depends on the multipath components' magnitude and timing difference with the LOS path. For VLP, $K$ also influences the magnitude and the spatial extent of the NLOS-induced positioning errors, as attested by the bottom row of Fig. 8. For VLP, the optimal $K$ strongly varies with the optical propagation factors, of which LOS blockage (large-scale fading) is an example. No generally applicable guidelines can be derived based on the, in this manuscript, performed measurements.

On the basis of this Section IV-C, a CIR- (for UWB) or a rule-based (for VLP) dynamic anchor selection is advocated for, in place of employing a fixed, roll-out-dependent $K$.

*2) Influence of the Calibration Process:* So far, to ensure scalability, the calibration effort to counteract bias is consciously constrained to the feasible minimum. Unfortunately, this limits the achievable accuracy. A calibration effort-accuracy tradeoff exists.

With adequate antenna delay-type calibration, only relying on one to a few measurement(s) that can be collected with a single off-site setup, UWB's $\hat{d}_i$ underestimation can be counteracted. With uniform and anchor-individual bias compensation, emulated by adding Section IV-A4's mean ranging error data, the KF-based $p_{50}/p_{90}$ gain at height 1 in LOS amounts to 10%/11% (to 4.3/8.3 cm) and 23%/25% (3.6/6.9 cm), respectively. The former is feasible to a certain degree as it only requires the bias values of a statistically significant batch of transceiver pairs. The latter is impractical for large-scale UWB roll-outs. Accuracy-prioritizing applications would furthermore wield the measurements to fit a more complex $\widehat{d}_i - d_i$ compensation curve. The UWB bias can be well modeled as linear (with a 1-1.1 slope). The $p_{50}/p_{90}$ then reduces to 3.3/6.2 cm, and in the uniform case to 4.1/8.1 cm.

In RSS-based VLP, the variability in the transmitter response, which typically vastly exceeds that of both in between PDs and between the physical and tabulated characteristics, warrants the use of a well-characterized reference receiver to preferably *a priori* calibrate each LED's $P_{t,i}$. Especially for this cheap and not-optimized transmitter, assuming a common median $P_{t,i}$ worsens the $p_{50}/p_{90}$ substantially to 13.8/45.7 cm. Only with on-site calibration measurements, for which supplying the ground truth is a daunting task, can the $\widehat{d}_i$-dependent bias including transmitter tilt be captured. Importantly, VLP needs a more elaborate calibration than UWB to deliver the (half)decimeter-order positioning.

All in all, for the systems at hand, the associated calibration effort growth prohibits striving for an enlarged accuracy.

## V. Conclusion and Future Work

This manuscript benchmarked the 2-D positioning performance of aSDS-TWR UWB and RSS-based (u)VLP in LOS and various NLOS conditions, based on abundant positioning data that were collected across a substantial 8 m by 6 m evaluation area with respect to a highly accurate ground-truth system. In a LOS-dominated environment, both UWB and VLP ensure accurate localization. The median $p_{50}$

and 90th percentile $p_{90}$ positioning errors lie in the order of 5 and 10 cm, respectively. With their typical roll-outs, obstacle-induced path loss and multipath-based ranging outliers are more spatially confined for (u)VLP than for UWB. As a consequence, VLP manages a decimeter-order $p_{90}$, even near the obstacles, while UWB displays a $p_{90}$ in the 10–20-cm range. Attaining a $p_{50} = 21.3$ cm at a 25-Hz update rate demonstrated uVLP's viability outside a lab environment.

The future work consists both of extending the (u)VLP-UWB comparison to more strenuous environments (i.e., with human body blockage, outage and storage racks) and to 3-D drone applications (i.e., with tilt and a significant velocity). Moreover, the potential accuracy improvement of sensor fusion, e.g., with inertial measurements in NLOS conditions, will need to be investigated. The set of sensors should be tailored to the engineering budget of the targeted application. The latter study area can also entail combined (u)VLP and UWB localization.

## List of Abbreviations

| | |
|---|---|
| *2-D* | Two-dimensional |
| *3-D* | Three-dimensional |
| *AOA* | Angle of arrival |
| *aSDS-TWR* | Asymmetric double-sided two-way ranging |
| *CF* | Characteristic frequency |
| *CIR* | Channel impulse response |
| *DC* | Direct current |
| *DTW* | Dynamic time-warped trajectory |
| *FD* | Discrete Fréchet distance |
| *FDMA* | Frequency-division multiple access |
| *h1* | Receiver height 1, approx. 0.5 m |
| *h2* | Receiver height 2, approx. 1.15 m |
| *IIoT* | Industrial Internet of Things |
| *IoT* | Internet of Things |
| *IPS* | Indoor Positioning System |
| *K* | Number of selected anchors |
| *KF* | Extended (UWB) or linear (VLP) Kalman filter |
| *LaaS* | Light(ing) as a Service |
| *LED* | Light-emitting diode |
| *LOS* | Line-of-sight |
| *LSOOP* | Light signals of opportunity |
| *MBF* | Model-based fingerprinting |
| *MLAT* | Multilateration |
| *MoCap* | Motion capture |
| *NLOS* | Non-line-of-sight |
| $p_{50}$, $p_{75}$, $p_{90}$, $p_{95}$ | 50th, 75th, 90th, 95th percentile of the 2-D positioning error |
| $p_{50,N}$, $p_{75,N}$ $p_{90,N}$, $p_{95,N}$ | $p_{50}$, $p_{75}$, $p_{90}$, $p_{95}$ variants only considering 1 m bounding box data around obstacles |
| *PD* | Photodiode |
| *PDA* | Thorlabs' PDA36A2 |
| *QPoS* | Quality of positioning service |
| *R* | Winding route trajectory |
| *RGB* | Additive of red, green and blue (sub)LEDs |
| *RSS* | Received signal strength |
| *SNR* | Signal-to-noise-ratio |
| *TDOA* | Time difference of arrival |
| *TOF* | Time of flight |
| *uVLP* | Unmodulated VLP |
| *UWB* | Ultra-wideband |
| *VLP* | Visible Light Positioning |
| *Z* | Zigzag trajectory. |

## Acknowledgment

This work was executed within the imec AAA UWB localization research project 75.

## References

[1] G. M. Silva, J. Torres-Sospedra, and J. Huerta, "A meta-review of indoor positioning systems," *Sensors*, vol. 19, no. 20, pp. 1–45, 2019, doi: 10.3390/s19204507.

[2] A. Basiri *et al.*, "Indoor location based services challenges, requirements and usability of current solutions," *Comput. Sci. Rev.*, vol. 24, pp. 1–12, May 2017, doi: 10.1016/j.cosrev.2017.03.002.

[3] A. Alarifi *et al.*, "Ultra wideband indoor positioning technologies: Analysis and recent advances," *Sensors*, vol. 16, no. 5, pp. 1–36, 2016, doi: 10.3390/s16050707.

[4] P. H. Pathak, X. Feng, P. Hu, and P. Mohapatra, "Visible light communication, networking, and sensing: A survey, potential and challenges," *IEEE Commun. Surveys Tuts.*, vol. 17, no. 4, pp. 2047–2077, 4th Quart., 2015, doi: 10.1109/COMST.2015.2476474.

[5] S. De Lausnay, L. De Strycker, J. Goemaere, N. Stevens, and B. Nauwelaers, "A visible light positioning system using frequency division multiple access with square waves," in *Proc. 9th Int. Conf. Signal Process. Commun. Syst. (ICSPCS)*, Cairns, QLD, Australia, 2015, pp. 1–7, doi: 10.1109/ICSPCS.2015.7391787.

[6] S. Bastiaens, K. Deprez, L. Martens, W. Joseph, and D. Plets, "A comprehensive study on light signals of opportunity for subdecimetre unmodulated visible light positioning," *Sensors*, vol. 20, no. 19, p. 5596, 2020.

[7] S. Bastiaens, W. Raes, N. Stevens, L. Martens, W. Joseph, and D. Plets, "Impact of a photodiode's angular characteristics on RSS-based VLP accuracy," *IEEE Access*, vol. 8, pp. 83116–83130, 2020, doi: 10.1109/ACCESS.2020.2991298.

[8] T. V. Haute *et al.*, "Platform for benchmarking of RF-based indoor localization solutions," *IEEE Commun. Mag.*, vol. 53, no. 9, pp. 126–133, Sep. 2015, doi: 10.1109/MCOM.2015.7263356.

[9] F. Potortì, A. Crivello, P. Barsocchi, and F. Palumbo, "Evaluation of indoor localisation systems: Comments on the ISO/IEC 18305 standard," in *Proc. Int. Conf. Indoor Position. Indoor Navig. (IPIN)*, Nantes, France, 2018, pp. 1–7, doi: 10.1109/IPIN.2018.8533710.

[10] M. Ridolfi, N. Macoir, J. V.-V. Gerwen, J. Rossey, J. Hoebeke, and E. De Poorter, "Testbed for warehouse automation experiments using mobile AGVs and drones," in *Proc. IEEE Conf. Comput. Commun. Workshops (INFOCOM WKSHPS)*, Paris, France, 2019, pp. 919–920, doi: 10.1109/INFCOMW.2019.8845218.

[11] F. Potortì, P. Barsocchi, M. Girolami, J. Torres-Sospedra, and R. Montoliu, "Evaluating Indoor Localization solutions in large environments through competitive benchmarking: The EvAAL-ETRI competition," in *Proc. Int. Conf. Indoor Position. Indoor Navig. (IPIN)*, Banff, AB, Canada, 2015, pp. 1–10, doi: 10.1109/IPIN.2015.7346970.

[12] N. Macoir *et al.*, "UWB localization with battery-powered wireless backbone for drone-based inventory management," *Sensors*, vol. 19, no. 3, pp. 1–18, 2019, doi: 10.3390/s19030467.

[13] B. Van Herbruggen *et al.*, "Wi-PoS: A low-cost, open source ultra-wideband (UWB) hardware platform with long range sub-GHz backbone," *Sensors*, vol. 19, no. 7, pp. 1–17, 2019, doi: 10.3390/s19071548.

[14] Z. Irahhauten, H. Nikookar, and G. J. M. Janssen, "An overview of ultra wide band indoor channel measurements and modeling," *IEEE Microw. Wireless Compon. Lett.*, vol. 14, no. 8, pp. 386–388, Aug. 2004, doi: 10.1109/LMWC.2004.832620.

[15] A. De Angelis, M. Dionigi, A. Moschitta, R. Giglietti, and P. Carbone, "Characterization and modeling of an experimental UWB pulse-based distance measurement system," *IEEE Trans. Instrum. Meas.*, vol. 58, no. 5, pp. 1479–1486, May 2009, doi: 10.1109/TIM.2008.2009204.

[16] F. Hartmann, F. Pistorius, A. Lauber, K. Hildenbrand, J. Becker, and W. Stork, "Design of an embedded UWB hardware platform for navigation in GPS denied environments," in *Proc. IEEE Symp. Commun. Veh. Technol. Benelux (SCVT)*, Luxembourg City, Luxembourg, 2015, pp. 1–6, doi: 10.1109/SCVT.2015.7374232.

[17] M. Ridolfi, J. Fontaine, B. Van Herbruggen, W. Joseph, J. Hoebeke, and E. De Poorter, "UWB anchor nodes self-calibration in NLOS conditions: A machine learning and adaptive PHY error correction approach," *Wireless Netw.*, vol. 27, no. 4, pp. 3007–3023, 2021, doi: 10.1007/s11276-021-02631-0.

[18] D. Dardari, A. Conti, U. J. Ferner, A. Giorgetti, and M. Z. Win, "Ranging with ultrawide bandwidth signals in multipath environments," *Proc. IEEE*, vol. 97, no. 2, pp. 404–426, Feb. 2009, doi: 10.1109/JPROC.2008.2008846.

[19] J.-Y. Lee and R. A. Scholtz, "Ranging in a dense multipath environment using an UWB radio link," *IEEE J. Sel. Areas Commun.*, vol. 20, no. 9, pp. 1677–1683, Dec. 2002, doi: 10.1109/JSAC.2002.805060.

[20] I. Guvenc and C.-C. Chong, "A Survey on TOA based wireless localization and NLOS mitigation techniques," *IEEE Commun. Surveys Tuts.*, vol. 11, no. 3, pp. 107–124, 3rd Quart., 2009, doi: 10.1109/SURV.2009.090308.

[21] A. R. J. Ruiz and F. S. Granja, "Comparing Ubisense, BeSpoon, and DecaWave UWB location systems: Indoor performance analysis," *IEEE Trans. Instrum. Meas.*, vol. 66, no. 8, pp. 2106–2117, Aug. 2017, doi: 10.1109/TIM.2017.2681398.

[22] I. Guvenc, C. Chong, and F. Watanabe, "NLOS identification and mitigation for UWB localization systems," in *Proc. IEEE Wireless Commun. Netw. Conf.*, Hong Kong, 2007, pp. 1571–1576, doi: 10.1109/WCNC.2007.296.

[23] H. Perakis and V. Gikas, "Evaluation of range error calibration models for indoor UWB positioning applications," in *Proc. Int. Conf. Indoor Position. Indoor Navig. (IPIN)*, Nantes, France, 2018, pp. 206–212, doi: 10.1109/IPIN.2018.8533755.

[24] A. D. Preter, G. Goysens, J. Anthonis, J. Swevers, and G. Pipeleers, "Range bias modeling and autocalibration of an UWB positioning system," in *Proc. Int. Conf. Indoor Position. Indoor Navig. (IPIN)*, Pisa, Italy, 2019, pp. 1–8, doi: 10.1109/IPIN.2019.8911815.

[25] H. Wymeersch, S. Marano, W. M. Gifford, and M. Z. Win, "A machine learning approach to ranging error mitigation for UWB localization," *IEEE Trans. Commun.*, vol. 60, no. 6, pp. 1719–1728, Jun. 2012, doi: 10.1109/TCOMM.2012.042712.110035.

[26] R. Maalek and F. Sadeghpour, "Accuracy assessment of ultra-wide band technology in locating dynamic resources in indoor scenarios," *Autom. Construct.*, vol. 63, pp. 12–26, Mar. 2016, doi: 10.1016/j.autcon.2015.11.009.

[27] P. Dabove, V. Di Pietra, M. Piras, A. A. Jabbar, and S. A. Kazim, "Indoor positioning using ultra-wide band (UWB) technologies: Positioning accuracies and sensors' performances," in *Proc. IEEE/ION Position Location Navig. Symp. (PLANS)*, Monterey, CA, USA, 2018, pp. 175–184, doi: 10.1109/PLANS.2018.8373379.

[28] Y. Zhuang *et al.*, "A survey of positioning systems using visible LED lights," *IEEE Commun. Surveys Tuts.*, vol. 20, no. 3, pp. 1963–1988, 3rd Quart., 2018, doi: 10.1109/COMST.2018.2806558.

[29] H. Yang, W.-D. Zhong, C. Chen, A. Alphones, and P. Du, "QoS-driven optimized design-based integrated visible light communication and positioning for indoor IoT networks," *IEEE Internet Things J.*, vol. 7, no. 1, pp. 269–283, Jan. 2020, doi: 10.1109/JIOT.2019.2951396.

[30] X. Liu, X. Wei, and L. Guo, "DIMLOC: Enabling high-precision visible light localization under dimmable LEDs in smart buildings," *IEEE Internet Things J.*, vol. 6, no. 2, pp. 3912–3924, Apr. 2019, doi: 10.1109/JIOT.2019.2893251.

[31] N. Stevens, "Bias introduced by true radiation patterns in RSS-based visible light positioning," in *Proc. IEEE SENSORS*, Montreal, QC, Canada, 2019, pp. 1–4, doi: 10.1109/SENSORS43011.2019.8956584.

[32] D. Plets, S. Bastiaens, L. Martens, W. Joseph, and N. Stevens, "On the impact of LED power uncertainty on the accuracy of 2D and 3D visible light positioning," *Optik*, vol. 195, Oct. 2019, Art. no. 163027, doi: 10.1016/j.ijleo.2019.163027.

[33] F. Alam, N. Faulkner, M. Legg, and S. Demidenko, "Indoor visible light positioning using spring-relaxation technique in real-world setting," *IEEE Access*, vol. 7, pp. 91347–91359, 2019, doi: 10.1109/ACCESS.2019.2927922.

[34] W. Raes, N. Knudde, J. De Bruycker, T. Dhaene, and N. Stevens, "Experimental evaluation of machine learning methods for robust received signal strength-based visible light positioning," *Sensors*, vol. 20, no. 21, p. 6109, 2020, doi: 10.3390/s20216109.

[35] Z. Li, A. Yang, H. Lv, L. Feng, and W. Song, "Fusion of visible light indoor positioning and inertial navigation based on particle filter," *IEEE Photon. J.*, vol. 9, no. 5, pp. 1–13, Oct. 2017, doi: 10.1109/JPHOT.2017.2733556.

[36] Y. Zhuang, Q. Wang, M. Shi, P. Cao, L. Qi, and J. Yang, "Low-power centimeter-level localization for indoor mobile robots based on ensemble kalman smoother using received signal strength," *IEEE Internet Things J.*, vol. 6, no. 4, pp. 6513–6522, Aug. 2019, doi: 10.1109/JIOT.2019.2907707.

[37] Q. Xu, R. Zheng, and S. Hranilovic, "IDyLL: Indoor localization using inertial and light sensors on smartphones," in *Proc. ACM Int. Joint Conf. Pervasive Ubiquitous Comput.*, Osaka, Japan, 2015, pp. 307–318, doi: 10.1145/2750858.2807540.

[38] C. Zhang and X. Zhang, "Visible light localization using conventional light fixtures and smartphones," *IEEE Trans. Mobile Comput.*, vol. 18, no. 12, pp. 2968–2983, Dec. 2019, doi: 10.1109/TMC.2018.2888973.

[39] Q. Van den Brande, S. Lemey, J. Vanfleteren, and H. Rogier, "Highly efficient impulse-radio ultra-wideband cavity-backed slot antenna in stacked air-filled substrate integrated waveguide technology," *IEEE Trans. Antennas Propag.*, vol. 66, no. 5, pp. 2199–2209, May 2018, doi: 10.1109/TAP.2018.2809626.

[40] M. Ridolfi *et al.*, "Experimental evaluation of UWB indoor positioning for sport postures," *Sensors*, vol. 18, no. 18, pp. 1–20, 2018, doi: 10.3390/s18010168.

[41] S. Bastiaens, S. K. Goudos, W. Joseph, and D. Plets, "Metaheuristic optimization of LED locations for visible light positioning network planning," *IEEE Trans. Broadcast.*, vol. 67, no. 4, pp. 894–908, Dec. 2021, doi: 10.1109/TBC.2021.3099734.

[42] R. Labbe. (2020). *Kalman and Bayesian Filters in Python*. [Online]. Available: https://github.com/rlabbe/Kalman-and-Bayesian-Filters-in-Python

[43] P. C. Chen, "A non-line-of-sight error mitigation algorithm in location estimation," in *Proc. IEEE Wireless Commun. Netw. Conf.*, vol. 1. New Orleans, LA, USA, Sep. 1999, pp. 316–320, doi: 10.1109/WCNC.1999.797838.

[44] Y.-T. Chan, W.-Y. Tsui, H.-C. So, and P.-C. Ching, "Time-of-arrival based localization under NLOS conditions," *IEEE Trans. Veh. Technol.*, vol. 55, no. 1, pp. 17–24, Jan. 2006, doi: 10.1109/TVT.2005.861207.

[45] J. Fan and A. S. Awan, "Non-line-of-sight identification based on unsupervised machine learning in ultra wideband systems," *IEEE Access*, vol. 7, pp. 32464–32471, 2019, doi: 10.1109/ACCESS.2019.2903236.

[46] V. Barral, C. J. Escudero, and J. A. García-Naya, "NLOS classification based on RSS and ranging statistics obtained from low-cost UWB devices," in *Proc. 27th Eur. Signal Process. Conf. (EUSIPCO)*, Sep. 2019, pp. 1–5, doi: 10.23919/EUSIPCO.2019.8902949.

[47] I. Guvenc, C. C. Chong, F. Watanabe, and H. Inamura, "NLOS identification and weighted least squares localization for UWB systems using multipath channel statistics," *EURASIP J. Adv. Signal Process.*, vol. 2008, no. 1, pp. 1–14, 2007, doi: 10.1155/2008/271984.

[48] V. Savic, E. G. Larsson, J. Ferrer-Coll, and P. Stenumgaard, "Kernel methods for accurate UWB-based ranging with reduced complexity," *IEEE Trans. Wireless Commun.*, vol. 15, no. 3, pp. 1783–1793, Mar. 2016, doi: 10.1109/TWC.2015.2496584.

[49] L. Schmid, D. Salido-Monzú, and A. Wieser, "Accuracy assessment and learned error mitigation of UWB ToF ranging," in *Proc. Int. Conf. Indoor Position. Indoor Navig. (IPIN)*, Pisa, Italy, Sep./Oct. 2019, pp. 1–8, doi: 10.1109/IPIN.2019.8911769.

[50] S. Maranò, W. M. Gifford, H. Wymeersch, and M. Z. Win, "NLOS identification and mitigation for localization based on UWB experimental data," *IEEE J. Sel. Areas Commun.*, vol. 28, no. 7, pp. 1026–1035, Sep. 2010, doi: 10.1109/JSAC.2010.100907.

**Sander Bastiaens** received the M.Sc. and Ph.D. degrees in electrical engineering from Ghent University, Ghent, Belgium, in 2017 and 2021, respectively.

Since 2017, he has been a member of the WAVES Research Group, Department of Information Technology, Ghent University/imec. His research is focused on visible light-based indoor positioning.

**Jono Vanhie-Van Gerwen** received the M.Sc. degree in computer science engineering from Ghent University, Ghent, Belgium, in July 2009.

Since August 2009, he has been working as a Research Engineer affiliated with the Department of Information Technology, Ghent University, where he is currently a Senior Research Engineer. His research activities have included performance analysis and benchmarking for wireless sensor networks, management and optimization of wireless testbeds, together with enabling them for experimentally driven education. In 2018, he received a professional drone pilot license and since he has been focused on indoor drone experimentation and automated operations.

**Nicola Macoir** received the M.Sc. degree in engineering in computer science from Ghent University, Ghent, Belgium, 2017.

He worked with the IDLab Research Group, Ghent University from 2017 to 2021, on providing advanced localization using ultrawide band technology. Since April 2021, he has been active as a Back-End Developer with RightCrowd, Ghent.

**Kenneth Deprez** received the M.Sc. degree in electronics and ICT engineering technology from Ghent University, Ghent, Belgium, in 2019, where he is currently pursuing the Ph.D. degree in active visible light positioning and passive visible light sensing of vehicles in tunnel environments.

In September 2019, he joined the WAVES Group, Department of Information Technology, Ghent University. His current research interests are localization and sensing of vehicles and humans based on visible light.

**Cedric De Cock** received the M.Sc. degree in electronics and ICT engineering technology from Ghent University, Ghent, Belgium, in 2020.

In 2020, he became a member of the imec-WAVES Group, Department of Information Technology, Ghent University. His research interests include IMU-enabled indoor positioning and signal processing.

**Wout Joseph** (Senior Member, IEEE) was born in Ostend, Belgium, on October 21, 1977. He received the M.Sc. degree in electrical engineering and the Ph.D. degree from Ghent University, Ghent, Belgium, in July 2000 and March 2005, respectively.

From September 2000 to March 2005, he was a Research Assistant with the Department of Information Technology, Ghent University. During this period, his scientific work was focused on electromagnetic exposure assessment. Since October 2007, he has been a Postdoctoral Fellow with the FWO-V (Research Foundation-Flanders), Brussel, Belgium. Since October 2009, he has been a Professor in the domain of "Experimental Characterization of Wireless Communication Systems." He has been an imec PI since 2017. His research work dealt with measuring and modeling of electromagnetic fields around base stations for mobile communications related to the health effects of the exposure to electromagnetic radiation. His professional interests are electromagnetic field exposure assessment, propagation for wireless communication systems, antennas, and calibration. Furthermore, he specializes in wireless performance analysis and Quality of Experience.

**Eli De Poorter** received the master's degree in computer science engineering from Ghent University, Ghent, Belgium, in 2006, and the Ph.D. degree from the Department of Information Technology, Ghent University in 2011.

He has been a Professor with the IDLab Research Group and imec, Ghent University since 2015. Since 2017, he has also been affiliated with the IMEC Research Institute. His team performs research on wireless communication technologies, such as (indoor) localization solutions, wireless IoT solutions, and machine learning for wireless systems and has over 200 publications in international journals or in the proceedings of international conferences. He is also a Co-Founder of the Lopos spin-off company, Ghent, which offers privacy-aware UWB safety solutions.

**David Plets** (Member, IEEE) received the M.Sc. degree in electrical engineering, and the Ph.D. degree from Ghent University, Ghent, Belgium, in 2006 and 2011, respectively.

In 2016, he became a Part-Time Professor in exposure to multiple physical agents in smart buildings. He is currently a member of the WAVES Group, Department of Information Technology, Ghent University. His current research interests include localization techniques and IoT, for both industrial and health-related applications. He is also involved in research on optimization of (cognitive) wireless communication networks, with a focus on coverage, interference, and exposure.